

Article

Development Characteristics and Reactivation Mechanism of a Large-Scale Ancient Landslide in Reservoir Area

Liang Dai¹, Chaojun Jia^{1,*}, Lei Chen¹, Qiang Zhang^{1,2} and Wei Chen³¹ School of Civil Engineering, Central South University, Changsha 410075, China² State Key Laboratory of Simulation and Regulation of Water Cycle in River Basin, Beijing 100048, China³ PowerChina Kunming Engineering Corporation Limited, Kunming 650000, China

* Correspondence: jiachaojun@csu.edu.cn

Abstract: The intricate geological conditions of reservoir banks render them highly susceptible to destabilization and damage from fluctuations in water levels. The study area, the Cheyipin section of the Huangdeng Hydroelectric Station, is characterized by numerous ancient landslides of varying scales and ages. In June 2019, during the reservoir filling process of the Huangdeng Hydroelectric Station, a large-scale reactivation of ancient landslides occurred in this area, posing severe threats to riverside infrastructure and human safety, including ground cracking, house cracking, foundation settlement, and road collapse. The reactivation mechanism of ancient landslides at reservoir banks is highly complex due to fluid dynamics. This study conducted field investigations in the Cheyipin landslide area, monitored surface and subsurface deformations using GNSS and inclinometers, and analyzed the distribution characteristics, destruction features, and reactivation mechanisms of the landslides through correlation analysis and numerical calculations. The results indicate that the instability pattern of the slopes manifests as traction-type sliding failure. The slopes do not slide along the ancient sliding surface but along a newly formed arcuate sliding surface, with the direct impact area mainly concentrated near the waterline. The stability of the slopes in this project is closely related to the reservoir water level. It can be assumed that the lowering of the reservoir water level triggered the reactivation of the ancient landslides in the Cheyipin section, while the influence of rainfall can be ignored. To prevent the reactivation of ancient landslides, attention should be focused on the changes in reservoir water level, avoiding rapid adjustments in water level during the initial lowering and final raising of the water level.

Keywords: ancient landslide; reservoir water level; rainfall; reactivation; failure mechanism; forensic study; numerical modeling



Citation: Dai, L.; Jia, C.; Chen, L.; Zhang, Q.; Chen, W. Development Characteristics and Reactivation Mechanism of a Large-Scale Ancient Landslide in Reservoir Area. *Appl. Sci.* **2024**, *14*, 3107. <https://doi.org/10.3390/app14073107>

Academic Editor: Tiago Miranda

Received: 28 February 2024

Revised: 29 March 2024

Accepted: 4 April 2024

Published: 8 April 2024



Copyright: © 2024 by the authors. Licensee MDPI, Basel, Switzerland. This article is an open access article distributed under the terms and conditions of the Creative Commons Attribution (CC BY) license (<https://creativecommons.org/licenses/by/4.0/>).

1. Introduction

The “Code for Investigation of Landslide Prevention and Control Engineering” (GB/T32864-2016) defines ancient landslides as those occurring before the Holocene, which remain stable as a whole [1]. Landslides occurring since the Holocene, which are currently stable as a whole, are termed old landslides. Both ancient and old landslides are only temporarily stable and may reactivate under certain natural or anthropogenic factors, such as seismic activity, rainfall, reservoir operations, and human activities [2–5]. The rapid development of hydraulic and hydroelectric engineering has brought substantial economic benefits but has also caused varying degrees of environmental damage around reservoir areas, leading to geological disasters such as landslides along the reservoir banks. The most notable event was the Vaiont landslide on 9 October 1963 [6–8]. Triggered by the periodic regulation of water levels and continuous rainfall, approximately 270 million cubic meters of the sliding mass on the left bank of the Vaiont Dam became unstable, resulting in the destruction of several downstream villages, the loss of over 2000 lives, and the abandonment of the entire reservoir.

Research indicates that within 1 to 3 years after the reservoir reaches its maximum water level, ancient and old landslides are prone to reactivation, and new landslides may occur [9]. Since the impoundment of the Three Gorges Dam in 2008, the reservoir water level has risen from 75 m to 175 m, resulting in significant changes to the geological environment. Several ancient landslides have been reactivated, leading to numerous disastrous consequences [10]. These landslides include the Qianjiangping landslide, the Huangduipo landslide, and the Shuping landslide, among others [11–13].

In early June 2019, multiple landslide events occurred within the territory of Huangdeng Reservoir in Lanping County, Yunnan Province [14]. According to on-site investigations, there are 26 large-scale landslides developed on both sides of the reservoir. The landslides are mainly composed of gravel, boulder, gravelly sandy soil, and gravelly sandy loam, with volumes ranging from hundreds of thousands to millions of cubic meters. Fourteen of these landslides are located below the normal reservoir water level, and their stability is significantly affected by reservoir impoundment. During normal reservoir operation, the water level fluctuates by up to 33 m, and the geological conditions of the reservoir banks are extremely complex, with some sections exhibiting poor stability. Due to the influence of fluid dynamics, the mechanism of landslide reactivation along the reservoir banks appears to be more complex [15]. Existing studies have been unable to effectively elucidate the reactivation mechanism of ancient landslides along reservoir banks [16].

The Cheyiping ancient landslide area in the Huangdeng Reservoir region is home to two villages with a total population of 268 people and currently has 1.18×10^5 m² of cultivated land. In order to prevent occurrences similar to the landslide sliding into the Three Gorges Reservoir, which could lead to more severe casualties and property losses [17], this study focuses on the Cheyiping ancient landslide in the Huangdeng Reservoir. Through a combination of field investigations, drilling engineering, and in situ monitoring, we analyze the developmental and deformational characteristics of the Cheyiping landslide. Additionally, we employ correlation analysis and numerical simulation to investigate the influencing factors and reactivation mechanism of ancient landslides, discussing the significant roles of reservoir water level fluctuations and rainfall in the reactivation of the Cheyiping ancient landslide. We anticipate that our study will provide further insights into the reactivation of ancient landslides, thereby offering important guidance for the prevention and mitigation of landslide geological disasters in this reservoir area.

2. Study Area

2.1. Study Area Setting

The Huangdeng Hydropower Station is situated in the upper reaches of the Lancang River in Lanping County, Yunnan Province, China, marking the sixth stage in the cascade development of the Lancang River from Quzika to Huangdeng (Figure 1). The Huangdeng Hydropower Station commenced operations with its first unit in June 2018, and the reservoir was impounded to its normal water level of 1619 m on 17 August 2018, with project completion in February 2019. The distribution of reservoir water levels and precipitation from January 2018 to April 2020 is depicted in Figure 2.

Dozens of ancient landslides are scattered along both banks of the river in this area. The Cheyiping ancient landslide, the subject of this study, is located on the left bank of the Lancang River, approximately 39 km downstream from the dam site of the Huangdeng Hydropower Station along the river road, representing a typical ancient landslide (Figure 3).

This landslide exhibits an overall planar profile that landslides eastward to the west, resembling a long “tongue”. The landslide is characterized by well-developed gullies, including three notably deep-cut gullies: 1# Gully (dry), 2# Gully (dry), and 3# Gully (perennial flow). The upstream boundary of the landslide extends from the steep bank on the right side of 2# Gully to the head of 1# Gully, and then to the ridge on the right side of Gully 1. The downstream boundary of the landslide mostly follows the course of 3# Gully. Both the upper and lower parts of the landslide exhibit distinct steep cuts, with heights ranging from approximately 1.5 m to 3 m, and display prominent shear cracks with varying

widths of 15 cm to 30 cm, locally exceeding 50 cm. The rear boundary is delineated by the exposed rock and soil interface of a sloping rock face, with an elevation of approximately 2290 m, and a steep wall height of about 20 m to 25 m. The steep wall displays large-scale joints with an orientation of N25° W and a dip angle of NE <80° to <85°. The landslide is approximately 450 m to 800 m wide in the north-south direction and about 1300 m long in the east-west direction. The distribution of the landslide body ranges in elevation from 1540 m to 2265 m, with a deposit thickness ranging from 23.8 m to 63.98 m. The exposed area of the landslide body is approximately 0.8 km², with an estimated volume of about 2000 × 10⁴ m³, categorizing it as a large landslide.

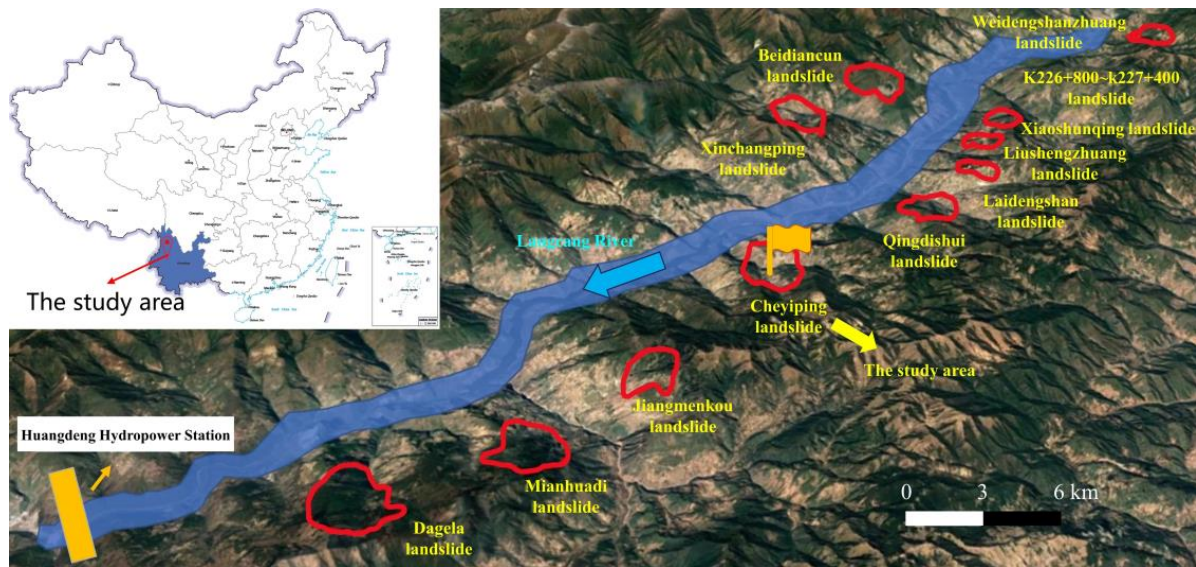


Figure 1. The study area.

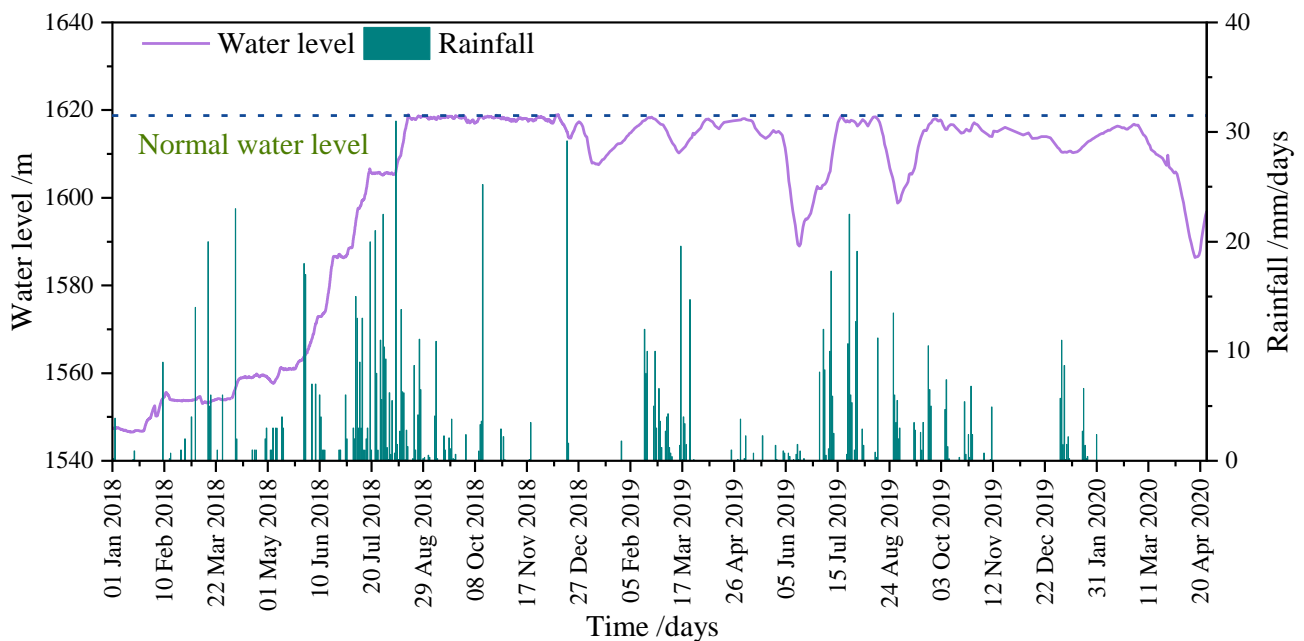


Figure 2. Reservoir water level and rainfall conditions in Huangdeng Reservoir.

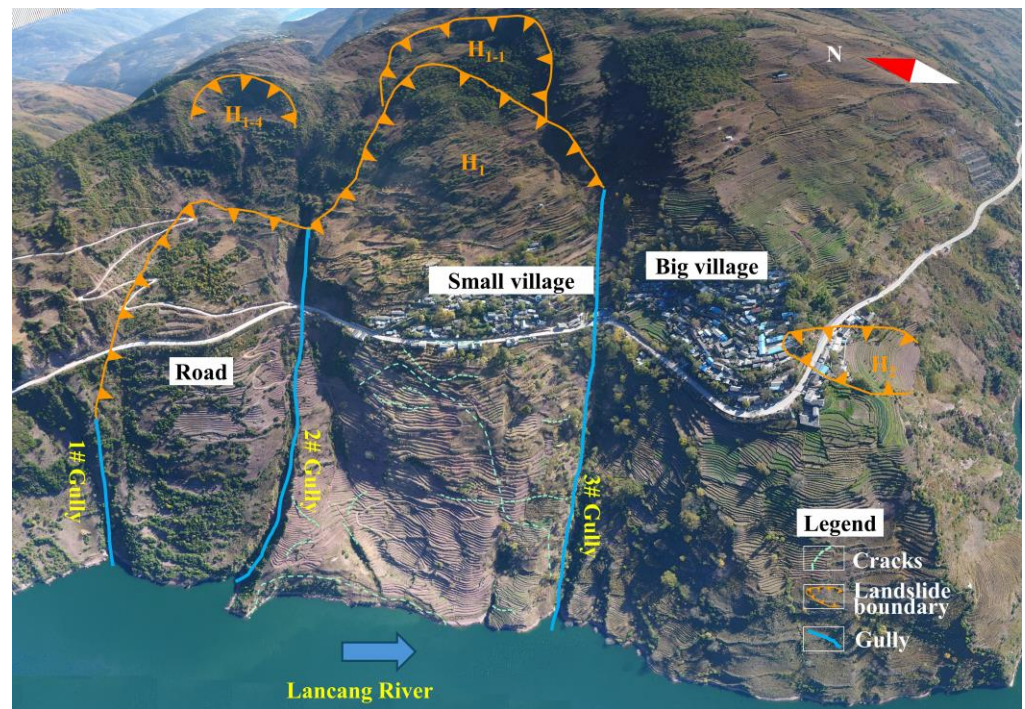


Figure 3. Cheyiping landslide in Huangdeng Reservoir.

2.1.1. Geological Structure

To investigate the geological conditions of the landslide, data from 22 new boreholes were utilized. The main geological profile of the landslide (Figure 4) was derived based on the stratigraphic conditions revealed by boreholes (Some typical geological conditions are shown in Figure 5) and the boundary. The Quaternary (Q) cover layer is widely distributed in Cheyiping village and its vicinity, underlain by the Middle Jurassic Huaikai Left Formation (J^{2h}). The bedrock primarily consists of purple-red laminated mudstone. The rock layers exposed at the surface exhibit significant tilting towards the open face (Lancang River, 2# Gully, 3# Gully and the major gully downstream of Cheyiping). The pre-tilting attitude of the exposed rock layers at the surface is $N20\text{--}30^\circ W$, $NE <20^\circ\text{--}35^\circ$, while boreholes reveal a dip angle of $5\text{--}10^\circ$ for the deeper rock layers. The slate rock mass exhibits a high degree of weathering, with completely weathered rock cores appearing as a mixture of soil and debris, while strongly weathered rock cores appear as fragments or debris.

The Quaternary deposits are categorized into three types based on their genesis: colluvial deposits (Q^{dl}), debris deposits (Q^{dl+col}), and landslide deposits (Q^{del}). The Q^{dl} deposits are remnants of the fourth-level terrace of the Lancang River, characterized by a layer of gray-yellow sand and gravel with a thickness ranging from 0.5 m to 1 m, primarily distributed near the lower part of the village road platform. The Q^{dl+col} deposits consist of gray-yellow and brown-yellow gravelly loam, sandy loam with embedded angular stones, and isolated stones. These deposits exhibit a moderate density, typically ranging from 5 m to 20 m in thickness. The stones are present in a skeletal form, with gaps filled with gravelly or gravelly loamy soil, and are widely distributed on most landslides in the entire study area. The gray-yellow and brown gravelly soil is primarily composed of gravel, angular stones, and sandy clay. The content of angular stones ranges from 20% to 40%, with diameters typically between 1 cm and 2 cm, with a few exceeding 5 cm. The main component is sandstone, with the soil's density ranging from loose to slightly dense. The soil's uniformity is poor, with thicknesses ranging from 23.8 m to 63.98 m, representing the deposits formed after the movement of the ancient landslide.

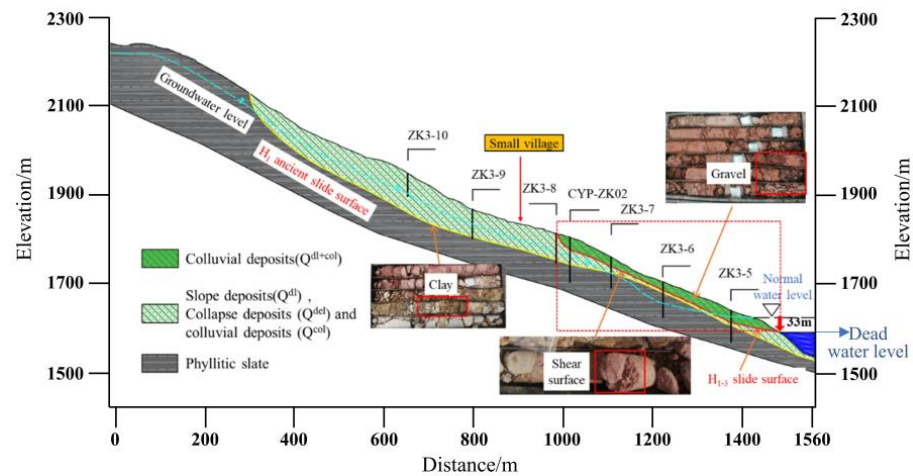


Figure 4. Geological profile of Cheyiping landslide.



Figure 5. Example of stratigraphic logs taken from a borehole realized in the site. (a) Strong toppling bedrock, (b) sliding mass (c) materials in the sliding zone.

The layer of soil in the sliding zone (Q^{del}) presents a predominant color palette of purple-red, gray-black, and brown-yellow. It is primarily composed of clay containing gravel interspersed with occasional fragments and gravel stones, the latter of which are sub-rounded. Notably, some sections of the sliding zone soil exhibit distinct mirror-like shear phenomena. The soil demonstrates a range of plasticity from malleable to rigid, with thicknesses typically ranging from 10 cm to 30 cm, although occasionally exceeding 50 cm. Multiple layers of this soil are distributed within the landslide body, indicating a history of multi-layered and multi-phase sliding deformations. Analysis of borehole data near the road and its upper section reveals different phases of sliding deformation occurring at depths around 60 m, 48 m, 40 m, 36 m, and 20 m. Boreholes located in the lower section of the road generally exhibit signs of sliding deformation at depths of 60 m, 50 m, 45 m, and 25 m.

2.1.2. Hydrogeological Conditions

The study area is characterized by a monsoon climate, exhibiting distinct dry and wet seasons. The rainy season typically spans from May to October, while the dry season lasts from November to April of the following year. The multi-year average temperature is 11.1 °C, with extreme maximum temperatures reaching 31.7 °C and extreme minimum temperatures dropping to −10.2 °C. The multi-year average precipitation is 973.5 mm, with an evaporation rate of 1645.2 mm and a relative humidity of 74%. The multi-year average wind speed is 1.6 m/s, with a maximum wind speed of 16.3 m/s, predominantly from the SSW direction.

The groundwater in this region primarily derives its recharge from atmospheric precipitation, ultimately discharging into the Lancang River, which serves as the area's lowest drainage reference. Within the landslide area of Cheyipin, groundwater is predominantly composed of water seeping from fractures in the bedrock and water within the pores of the loose layers of the Quaternary system. The sliding zone soil of Cheyiping landslide

exhibits the development of multiple relatively impermeable layers. Observations at the borehole sites reveal that some cores near the sliding surface are notably moist, indicating a higher soil moisture content. Analysis suggests the presence of stagnant water near the upper sliding surface of the Cheyiping landslide.

The Lancang River and the downstream of Cheyiping village are deeply incised by gullies. The depth of the incision in the upstream gully (2# Gully) of Cheyiping village reaches over 30 m, yet no groundwater is exposed, indicating that the groundwater level is buried deeply, constituting deep-seated fractured rock water. The water flow in 3# Gully originates from irrigation in Cheyiping village and from the water channel in the river. Seepage points have been observed in the central part of the landslide in front of the small village, primarily due to water infiltration from the channel, which then percolates underground for a short distance before seeping out onto the surface. During the exploration process, a water injection test was conducted. According to the “Geological Exploration Code for Hydropower Engineering” (GB50287-2016) [18], the permeability of rock and soil varies from large to small from the borehole to the bottom of the hole. Permeability is largely influenced by the clay content, with the permeability coefficient of the cover layer ranging from 7.22×10^{-7} to 9.82×10^{-5} m/s, indicating medium to weak permeability. The permeability coefficient of strongly weathered mudstone ranges from 8.08×10^{-7} to 2.17×10^{-6} m/s, indicating weak permeability.

2.1.3. Physical and Mechanical Properties of Landslide Materials

The physical and mechanical properties of both the landslide deposit and the slip surface were determined through experimentation. Samples for testing were obtained from rock outcrops and drill cores. The mass and volume of these samples were measured using an electronic balance and caliper, respectively, to calculate their natural density. Subsequently, triaxial compression tests were conducted on both saturated and natural samples to ascertain the cohesive and frictional angles. In situ shear tests were performed on all debris slips on the main body’s shallow surface to determine their cohesion and friction angle. For the underground portion of the landslide body and the shear band of the debris chute, laboratory direct shear tests were carried out on samples extracted from drill cores to establish the shear strength parameters. The unit weight of the debris was measured using an electronic balance and a dimensionally fixed aluminum box. The porosity of the debris soil was measured using a specific gravity bottle, and moisture content was determined using the oven-drying method. Table 1 provides values, it is notable that the shear strength of both the main body and shear band materials significantly decreases when saturated, while the porosity of the landslide material remains considerable.

Table 1. Mechanical parameters of the materials.

Materials	Porosity (%)	Water Content (%)	Natural	Saturated	Cohesion (kPa)	Frictional Angle (°)	Saturated	
			Unit Weight (kN/m ³)				Cohesion (kPa)	Frictional Angle (°)
Sliding body	12	12.7	19	20	16	24	15	23
Slip belt	14	13	18	19	23	25	21	23
Bedding rock	8	9	25	26	650	41	550	39

2.2. Characteristics of the Landslide

2.2.1. Historical Reactivation

Following the field geological survey and analysis of exploration findings, it has been observed that, since the reservoir’s impoundment in the 1950s, the ancient landslide at Cheyiping has undergone two distinct secondary sliding or deformation occurrences. These events are characterized by the emergence of two relatively minor secondary landslides, both macroscopically visible at the original rear edge of the landslide and within the accumulated mass (Figure 6). Specific descriptions are detailed below.

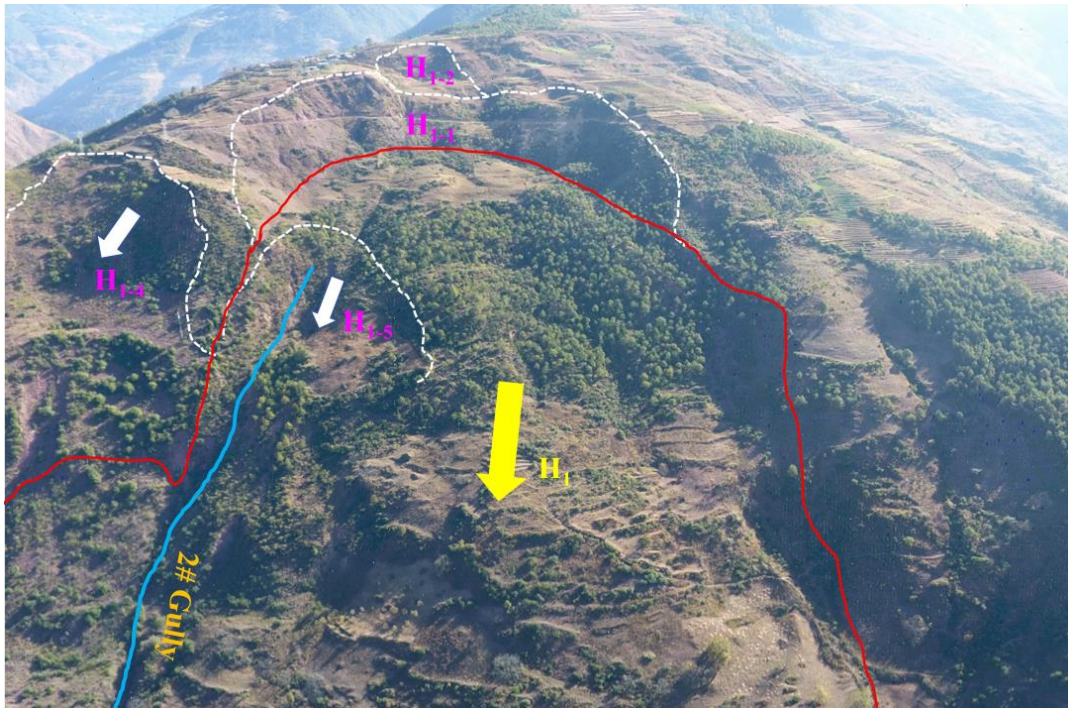


Figure 6. Topography of the rear edge of the H_1 landslide: the positions and boundaries of H_{1-1} , H_{1-2} , H_{1-4} , and H_{1-5} .

The H_{1-1} Landslide is situated at the rear edge of the Cheyiping ancient landslide deposit (H_1). According to field surveys, this landslide experienced a sliding event in 1956, resulting in a steep cliff forming at an elevation of approximately 2230 m and a landslide platform near the elevation of 2166 m. The platform, which is approximately 10 m to 20 m wide, is discontinuously incised by gullies in its central portion. Currently, the platform is fallow land. The rear edge of the landslide exhibits an arcuate shape, with a lateral width of about 200 m and a longitudinal length of about 150 m, distributed between elevations of 2175 m and 2250 m. The estimated thickness ranges from 10 m to 20 m, with a preliminary volume estimate of approximately $45 \times 10^4 \text{ m}^3$.

The H_{1-2} Landslide is situated at the rear edge of the Cheyiping ancient landslide deposit (H_1). Field investigations reveal that, following heavy rain in 1992, the H_{1-1} landslide expanded upwards due to excavation and cutting of the upper rural road on the landslide body. A sliding event occurred at the rear edge cliff formed by the 1956 movement, creating a new steep landslide at an elevation of approximately 2300 m and two terraces with a height difference of 5 m at an elevation of around 2282 m. The upper terrace is approximately 20 m wide, mostly continuous and intact, with slight discontinuity at the head of the gully, while the lower terrace is about 30 m wide. The landslide platform exhibits a circular-chair and tongue-shaped pattern, with a lateral width of about 50 m to 100 m, distributed between elevations of 2215 m and 2265 m, and a longitudinal length of approximately 120 m. The estimated thickness ranges from 5 m to 15 m, with a preliminary volume estimate of about $10 \times 10^4 \text{ m}^3$.

Additionally, two smaller landslides (H_{1-4} , H_{1-5}) are situated behind the Cheyiping ancient landslide mass along the roadway (Figure 6). These two landslides exhibit a pronounced “circular-chair” topography, characterized by steep cliffs at elevations ranging from 2130 m to 2150 m and a landslide platform near 2100 m. The width of the platform ranges from approximately 10 m to 20 m. Both landslides’ rear edges form an arc, with a width of about 150 m, a length of approximately 100 m, and an estimated thickness of 10 m to 20 m, with a preliminary volume estimate of about 15 to $25 \times 10^4 \text{ m}^3$.

2.2.2. Reactivations after Reservoir Impoundment

The H_{1-3} Landslide is situated at the leading edge of the Cheyiping ancient landslide deposit (H_1), representing a recent landslide formation resulting from the reservoir impoundment process of the Huangdeng Hydropower Station (Figure 7). This landslide's direction of movement extends approximately 150 m to 200 m, with a water length at the front edge of about 200 m to 250 m. Data from drilling and deep monitoring (ZK3-1) indicate a depth of 33.0 m for the bottom sliding surface, suggesting a thickness of the sliding mass ranging from 10 m to 35 m, with an estimated volume of approximately $60 \times 10^4 \text{ m}^3$.

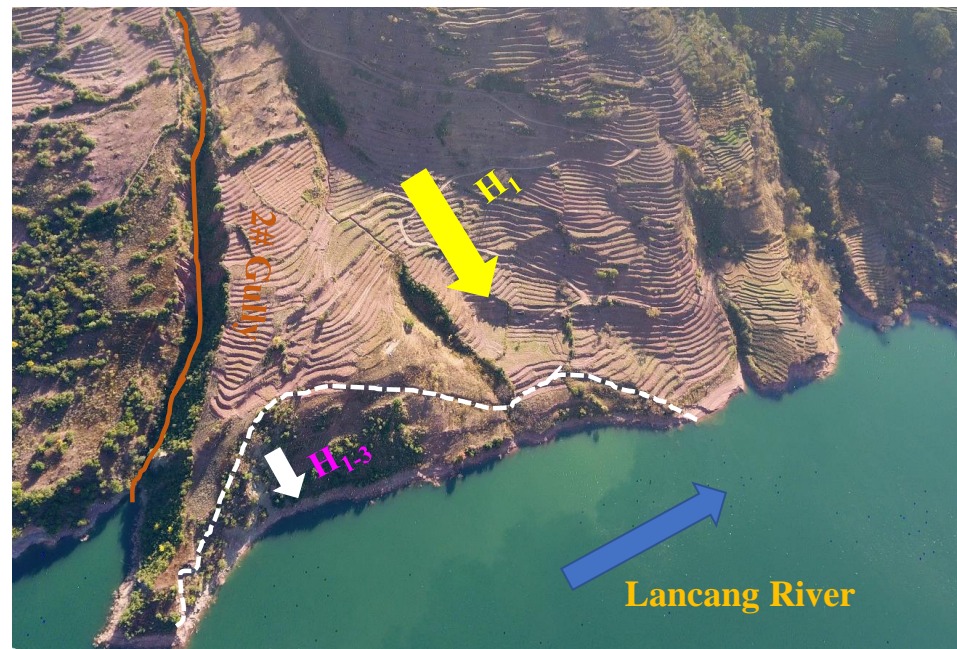


Figure 7. The new landslide H_{1-3} formed at the front edge of the landslide due to reservoir water level fluctuations.

The topographic features of the landslide are distinct, with an arc-shaped boundary creating a circular-chair terrain. The landslide's distribution spans elevations from 1619 m to 1660 m, with a primary sliding direction of approximately 285° . The landslide axis is nearly perpendicular to the Lancang River. The front edge's shear outlet has been submerged by reservoir waters. At an elevation of around 1660 m, the rear edge exhibits development of tension cracks and terraces, with crack widths ranging from 0.3 m to 1 m and terrace height differences from 0.5 m to 1.5 m, indicative of depths from 1 m to 2 m. Following the reservoir impoundment of the Huangdeng Hydropower Station in November 2017, the front edge of the Cheyiping ancient landslide was reactivated due to reservoir water influence. The current state of the landslide indicates it is in a stage of creep deformation, existing in a quasi-stable to unstable condition. Under unfavorable conditions, there is a high likelihood of further deformation and damage to the landslide.

2.3. Characteristics of Crack Development

The field investigation reveals the presence of 27 primary cracks, with LF4, LF8, and LF13 exhibiting relatively longer extensions compared to the others. The distribution of major landslide cracks is illustrated in Figure 8, and their characteristics are detailed in Table 2, with typical crack photos shown in Figure 9. Specifically, LF1 to LF20 are located below the river road and are mainly within the H_{1-3} landslide body, resulting from a sudden drop in the reservoir water level. Conversely, LF21 to LF27 are situated above the river road, mostly at the rear of the H_{1-3} landslide body, and were formed prior to the reservoir impoundment, showing a lesser correlation with the reservoir water level fluctuation.

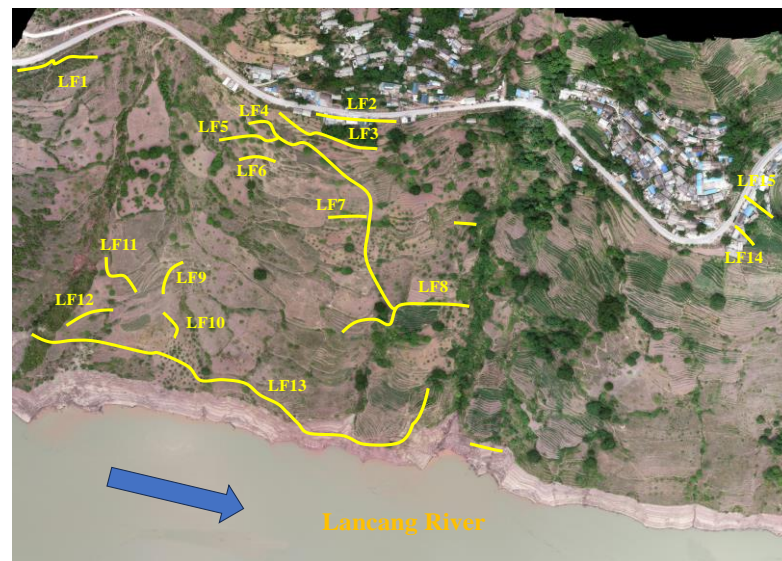


Figure 8. Distribution of cracks in Cheyiping reservoir section.

Table 2. Distribution and characteristics of cracks.

No.	ID	Elevation (m)	Location	Date	Strike	Length (m)	Width (cm)	Dislocation (cm)	Crack Type
LF1	CYP04	1807	Small village	June 2019	N30° W	120	5	0.3	Tensile
	CYP05	1804	upstream		N35° E		21	10	Tensile
	CYP06	1800	Below the road		N5° E		16	9	Tensile
LF2	CYP08	1807	Road foundation	June 2019	N50° E	95	2.5	1.5	Tensile
	CYP30	1807			N14° E		3	0.75	Tensile
LF3	CYP09	1800	Below the road	June 2019	N50° E	120	20	1.5	Tensile
	CYP10	1795			N56° E		25	5	Tensile
LF4	CYP11	1785	H ₁₋₃ trailing edge	June 2019	N5° W	360	1.5	0.75	Tensile
	CYP16	1773			N56° E		50	70	Tensile
	CYP17	1759			N59° E		40	40	Tensile
	CYP12	1779			N21° E		12	3.5	Tensile
LF5	CYP13	1774	H ₁₋₃ trailing edge	June 2019	N40° E	90	9	15	Tensile
	CYP14	1768			N15° E		4	2.5	Tensile
LF6	CYP15	1768	H ₁₋₃ trailing edge	June 2019	N13° E	40	30	7.5	Tensile
LF7	CYP18	1750	H ₁₋₃ trailing edge	April 2020	N30° E	50	11	2.5	Tensile
LF8	CYP25	1674	H ₁₋₃ middle part	June 2019	NW	195	6	1.5	Tensile
	CYP26	1684			SN		60	20	Tensile
	CYP27	1693			N6° W		30	50	Tensile
	CYP28	1694			N34° E		40	20	Tensile
LF9	CYP19	1679	H ₁₋₃ front edge	June 2019	N50° W	50	3	1.5	Tensile
LF10	CYP24	1657	H ₁₋₃ front edge	June 2019	N14° E	40	25	1.5	Tensile
CYP20	1683	N10° W			10		1.5	Tensile	
CYP21	1688	N70° W			80		1.5	2	Tensile
LF12	CYP22	1676	H ₁₋₃ front edge	June 2019	N45° W	50	10	2	Tensile
LF13	CYP23	1656	H ₁₋₃ front edge	June 2019	N39° W	450	3.5	1.5	Tensile
LF14	CYP31	1805	Retaining wall of road	April 2020	N46° E	25	7.5	2	Tensile
LF15	CYP32	1807	Road surface	April 2020	N30° E	70	23	7.5	Tensile
LF21	-	2278	H ₁ trailing edge	April 2020	SN	30	15	20	Tensile
LF22	-	2256	H ₁ side edge	1992	N74° W	40	10	5	Shear
LF24	-	2240	H ₁ side edge	1992	N58° E	50	5	1.5	Shear
LF26	-	2113	H ₁ side edge	1956	-	70	35	35	Shear
LF27	-	2080	H ₁ side edge	1956	-	90	20	100	Shear

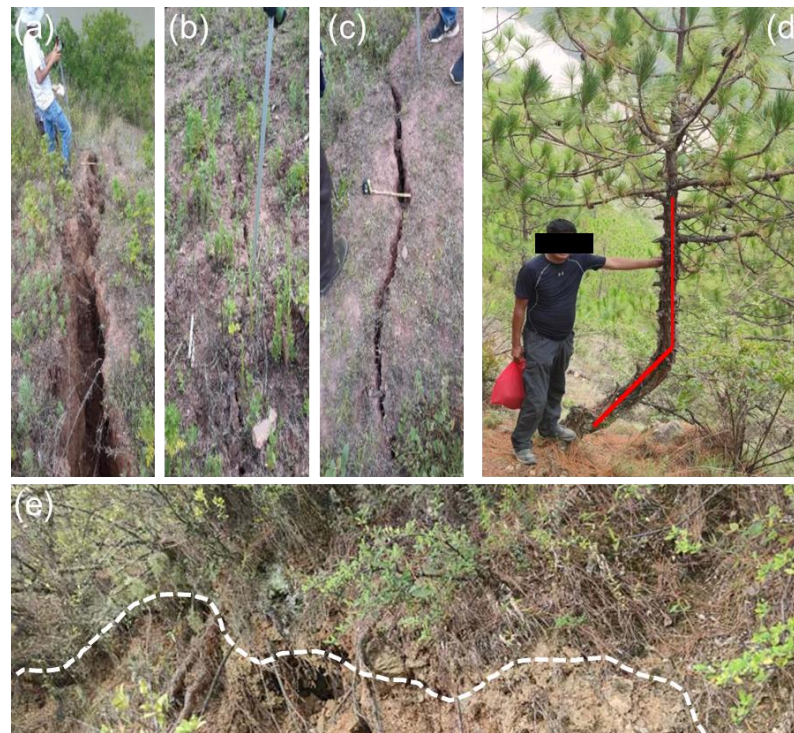


Figure 9. Characteristics of cracks induced by reservoir water level changes and old cracks in ancient landslides: (a–c) characteristics of tensional cracks; (d) Sabre-shaped trees developed near LF19; (e) photo of LF19 crack. (The red lines indicate the bending of the tree; The white dashed lines show the shape of the crack edges.)

2.3.1. Historical Reactivation

Cracks in the ancient landslide are mainly found in the upper to middle sections of its rear and downstream edges. These cracks exhibit characteristics of tensional shear, with some accompanied by the formation of feather-like features. Their formation is primarily attributed to shear stress induced by the compression of the rock and soil mass in the upper landslide. This compression leads to stress alterations in the landslide, ultimately causing the emergence of these cracks.

2.3.2. Reactivations after Reservoir Impoundment

After the reservoir was impounded, in June 2019, developed cracks were primarily distributed near the front edge of the landslide body below the riverside road, consisting mainly of tensional cracks. These cracks are characterized by the influence of reservoir impoundment and water level fluctuations on the rock and soil mass in the lower part of the landslide. The detachment of the landslide soil in the lower part resulted in deformation, which in turn caused a certain degree of deformation in the upper landslide, leading to the appearance of cracks. Among them, the formation of crack LF13 was mainly due to dynamic changes in the reservoir water level, resulting in reservoir bank collapse cracks. Crack LF19, on the downstream side, is a boundary crack controlling the deformation of the landslide body. This crack formed earlier, and phenomena such as “Sabre-shaped trees” can be seen on the landslide surface (Figure 9). The sliding of the landslide body this time also caused some deformation of this crack, with noticeable falling of the rock and soil mass in the crack-development area. In some sections, the crack opening width reaches 30–50 cm, forming terraces about 1–2 m high. Cracks on the ground surface in this area are often accompanied by ground subsidence and shallow sliding of rock and soil mass. Their longitudinal section morphology is mostly circular-chair-shaped or arc-shaped. The number of cracks in this area will increase further with the deformation and sliding of

the low elevation sections near the river, indicating a possibility of further enlargement of the deformation.

3. Research Methods

3.1. Landslide Surface Deformation Measurements

To measure the surface deformation of the landslide, two monitoring sections were established at the Cheyiping small village landslide body (H1) and the large village landslide body (H2), each with two monitoring points, totaling six GNSS monitoring points (Figures 2 and 3). Points CYP-GTP-01, CYP-GTP-02, and CYP-GTP-03 are located in the middle and lower parts of the H1 landslide body, while points CYP-GTP-04, CYP-GTP-05, and CYP-GTP-06 are situated within the H2 landslide body. The specific locations are shown in Figure 10.

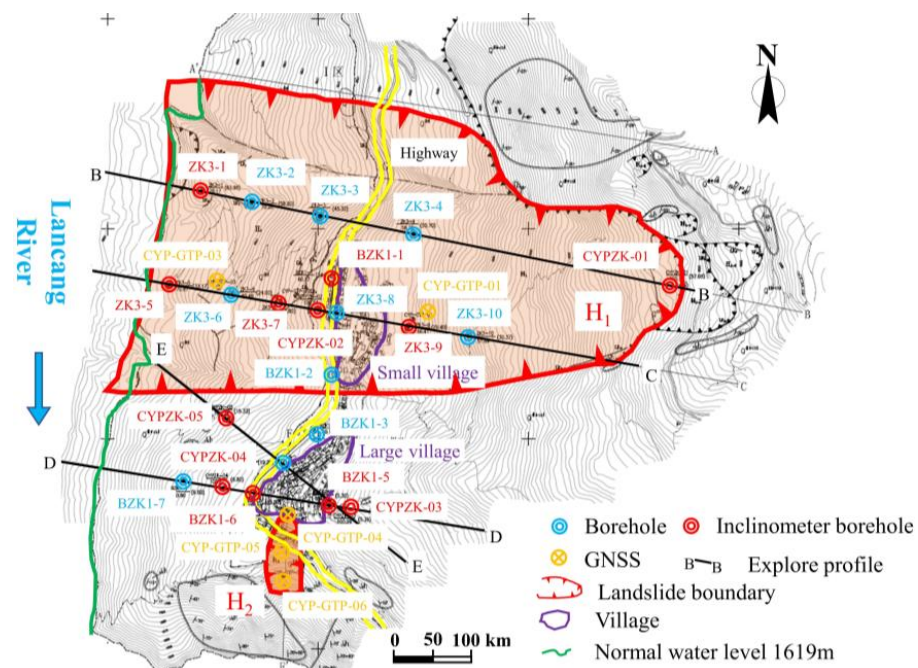


Figure 10. The layout of monitoring points for the Cheyiping landslide.

3.2. Measurement of Subsurface Deformation of Landslide

To measure the subsurface deformation of the landslide, 12 inclinometer boreholes were established at the Cheyiping landslide. Four inclinometer boreholes (ZK3-1, ZK3-5, ZK3-7, ZK3-9) were installed in the reservoir section of the Cheyipan landslide (H1). These boreholes primarily monitored the deep-seated deformation of the reservoir edge and the shore landslide of the Cheyipan village. Three inclinometer boreholes (BZK1-1, BZK1-5, BZK1-6) were deployed. The five deep boreholes (CYP-ZK01~CYP-ZK05) installed in the supplementary investigation phase. The inclinometer instruments used had a range of $\pm 15^\circ$ and an accuracy of 0.01 mm/500 mm. The specific locations are shown in Figure 10.

3.3. Testing of Physical and Mechanical Properties of Landslide Materials

The physical and mechanical properties of both the landslide deposit and the slip surface were determined through experimentation. Samples for testing were obtained from rock outcrops and drill cores. The mass and volume of these samples were measured using an electronic balance and caliper, respectively, to calculate their natural density. Subsequently, triaxial compression tests were conducted on both saturated and natural samples to ascertain the cohesive and frictional angles. In situ shear tests were performed on all debris slips on the main body's shallow surface to determine their cohesion and friction angle. For the underground portion of the landslide body and the shear band

of the debris chute, laboratory direct shear tests were carried out on samples extracted from drill cores to establish the shear strength parameters. The unit weight of the debris was measured using an electronic balance and a dimensionally fixed aluminum box. The porosity of the debris soil was measured using a specific gravity bottle, and moisture content was determined using the oven-drying method.

3.4. Correlation Analysis

3.4.1. Pearson Correlation Analysis

The Pearson correlation coefficient is defined as the covariance of two variables divided by the product of their standard deviations [19]. The formula is defined as follows:

$$r = \frac{\sigma_{xy}}{\sqrt{\sigma_x^2 \sigma_y^2}} \quad (1)$$

In Equation (1), r represents the correlation coefficient; σ_x represents the standard deviation of variable X ; σ_y represents the standard deviation of variable Y ; and σ_{xy} represents the covariance between variables X and Y . The value of r ranges between -1 and 1 , denoted as $|r| \leq 1$. A value of $|r|$ closer to 1 indicates a higher degree of correlation between the variables X and Y . When $|r| \geq 0.8$, the variables are highly correlated. When $0.5 \leq |r| < 0.8$, the variables are moderately correlated. When $0.3 \leq |r| < 0.5$, the variables are lowly correlated. When $|r| < 0.3$, the variables have a weak correlation and are essentially unrelated [20].

Due to the rising and falling of the reservoir water level, the following criteria are established for calculating the correlation between the reservoir water level and the cumulative displacement of the landslide.

During the rising phase of water levels, a positive correlation exists between monthly increases in water level and differences in monthly cumulative displacement. A higher correlation coefficient (r) signifies a stronger relationship, indicating that larger monthly increases in water level correspond to greater cumulative displacement of the landslide. Conversely, during the decreasing phase of reservoir water levels, a positive correlation between monthly decreases in water level and differences in monthly cumulative displacement occurs when the correlation coefficient (r) is negative. In this scenario, a higher absolute value of r suggests that larger monthly decreases in water level correspond to greater cumulative displacement, while a smaller absolute value indicates the opposite.

3.4.2. Net Correlation Analysis

Net correlation analysis refers to the examination of the correlation between two variables while controlling for the influence of other variables that may affect both. The resulting correlation coefficient is termed the net correlation coefficient [21]. In this study, we focus on analyzing the correlation between landslide deformation and reservoir water level. However, since rainfall during the period also affects landslide deformation, analyzing only the influence of reservoir water level on landslide deformation may not accurately reflect their complex relationship.

To mitigate the influence of rainfall on the relationship between water level and deformation, we control for the rainfall variable. The formula is as follows [22]:

$$r_{12-3} = \frac{r_{12} - r_{13}r_{23}}{\sqrt{(1 - r_{13}^2)(1 - r_{23}^2)}} \quad (2)$$

In Equation (2), r_{12-3} denotes the net correlation coefficient between variables 1 and 2 when variable 3 is controlled. r_{12} represents the Pearson correlation coefficient between variables 1 and 2. r_{13} stands for the Pearson correlation coefficient between variables 1 and 3. r_{23} represents the Pearson correlation coefficient between variables 2 and 3. The

net correlation coefficient r_{12-3} aligns in level of relevance and direction with the Pearson correlation coefficient r .

3.5. Stability Analysis of the Landslide

The GeoStudio 2018 R2 (version number: 9.1.1.16749) software, a Canadian geotechnical engineering analysis tool, was employed for landslide seepage simulation, stability analysis, and displacement calculation. The built-in SEEP/W module was utilized for landslide seepage simulation, while the built-in LANDSLIDE/W module was used for landslide stability analysis. The numerical computational model established is approximately 700 meters long and 400 meters high, as shown in Figure 11. For model grid division, a hybrid approach of triangular and quadrilateral elements was employed, considering both computational accuracy and convergence ease. The minimum size of the model elements was controlled at 5 m. The model consisted of a total of 2480 grid elements and 2535 grid nodes.

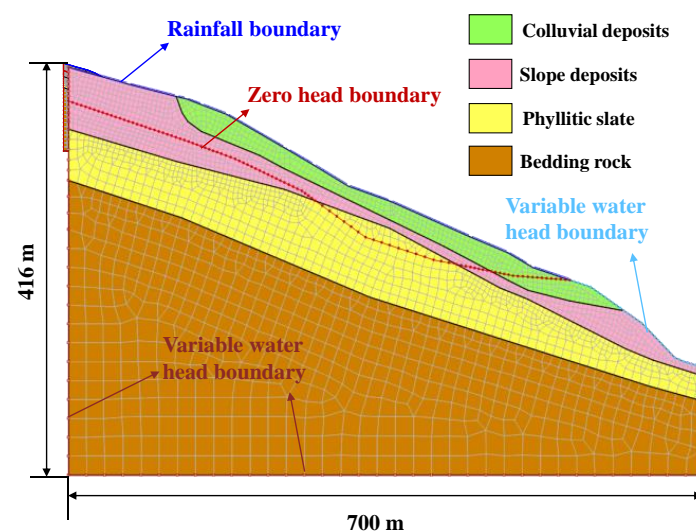


Figure 11. Illustrative diagram of the model's grid division and computational boundaries.

Based on geological surveys and laboratory experiments, the physical and mechanical parameters of the materials are presented in the Table 3. Knowing the saturated volumetric water content of different materials of the landslide body, the soil–water characteristic curve (SWCC) and the relationship curve between the permeability coefficient and matrix suction of the landslide body can be estimated and plotted using the Fredlund model function [23], as shown in Figure 12.

During the period from 2018 to 2022, the Huangdeng Hydropower Station recorded a maximum daily rainfall of approximately 30 mm. This data prompted analyses of reservoir bank landslide stability under two distinct scenarios: the influence of reservoir water level fluctuations alone and the combined effects of reservoir water level fluctuations and 30 mm/days rainfall.

Table 3. Material parameters in the numerical model.

Materials	Permeability Coefficient (m/s)	Unit Weight (kN/m ³)	Cohesion (kPa)	Frictional Angle (°)	Saturated Volumetric Moisture Content
Colluvial deposits	7.0×10^{-5}	18	16	22	0.26
Landslide deposits	8.98×10^{-5}	19	23	25	0.21
Phyllitic slate	1.16×10^{-5}	20	30	27	0.10
Bedding rock	5.79×10^{-7}	25	650	41	0.05

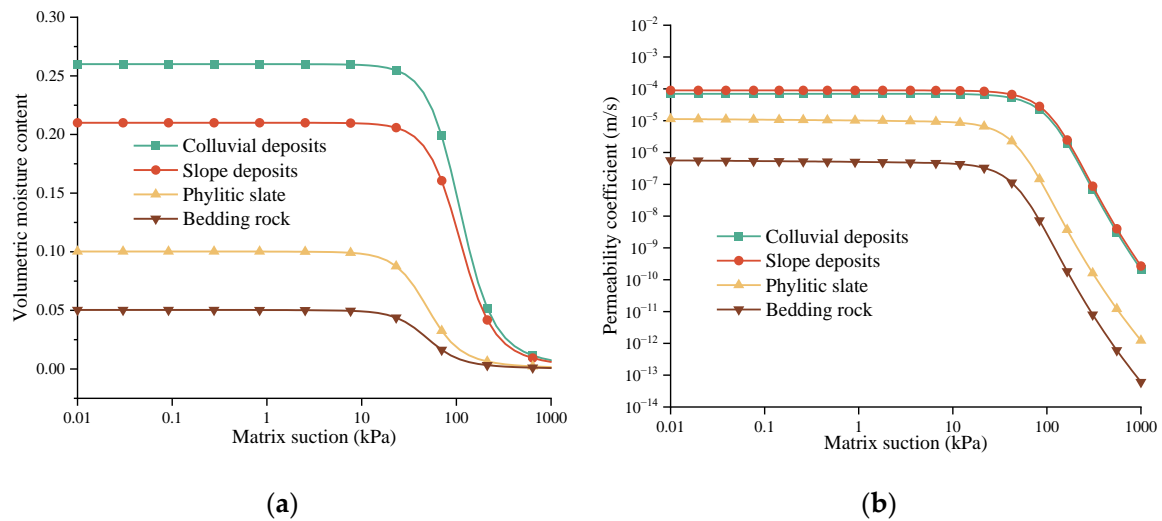


Figure 12. Soil-Water Characteristic Curve: (a) volumetric moisture content function; (b) permeability coefficient function.

4. Result

4.1. GNSS-Based Monitoring Data

The monitoring results are depicted in Figure 13, with Figure 13a illustrating the monitoring outcomes for horizontal surface displacement and Figure 13b showing the monitoring results for vertical surface displacement.

From Figure 13a, it is evident that significant horizontal convergence displacements occur at monitoring points CYP-GTP-02 and CYP-GTP-03. As of 20 September 2020, the horizontal convergence displacements were 1135.97 mm and 1054.68 mm, respectively. The daily displacement rates at CYP-GTP-02 ranged from -0.5 to 28.7 mm/day, with the maximum deformation rate occurring on 15 June 2019. Similarly, at CYP-GTP-03, the daily displacement rates ranged from -2.9 to 30.8 mm/day, with the maximum deformation rate also occurring on 15 June 2019.

From Figure 13b, it is evident that the monitoring points CYP-GTP-02 and CYP-GTP-03 also exhibit significant vertical displacement changes. As of 20 September 2020, the vertical displacements were 654.10 mm and 493.60 mm, respectively. The daily displacement rates at CYP-GTP-02 ranged from -8 to 23.8 mm/day, with the maximum deformation rate occurring on 13 June 2019. Similarly, at CYP-GTP-03, the daily displacement rates ranged from -12 to 16.4 mm/day, with the maximum deformation rate also occurring on 13 June 2019.

The monitoring data underscore that, during the continuous decrease in reservoir water level, points 2 and 3 exhibited significant horizontal displacements and deformation rates, clearly influenced by the declining water levels. As the water level gradually rose, the horizontal convergence displacements gradually stabilized. Consequently, it is imperative to closely monitor the deformation of this landslide section during the flood season and periods of substantial reservoir water level changes.

As of 20 September 2020, the cumulative horizontal displacement at CYP-GTP-01 was 350.41 mm, with a vertical displacement of 195.9 mm. The daily horizontal displacement rate ranged from -5.1 to 6.9 mm/day, and the daily vertical displacement rate ranged from -12 to 15 mm/day. The maximum deformation rates occurred on 19 June 2019, and 20 June 2019, respectively. Considering the soft lithology and the thick superficial deposits in this area, there is a certain degree of apparent deformation under natural conditions. Overall, the deformation is relatively smooth, with minimal changes in displacement rates during the intense reservoir level fluctuations, remaining within normal fluctuation ranges. Therefore, there is little correlation between the natural creep of the landslide deposit and reservoir level changes.

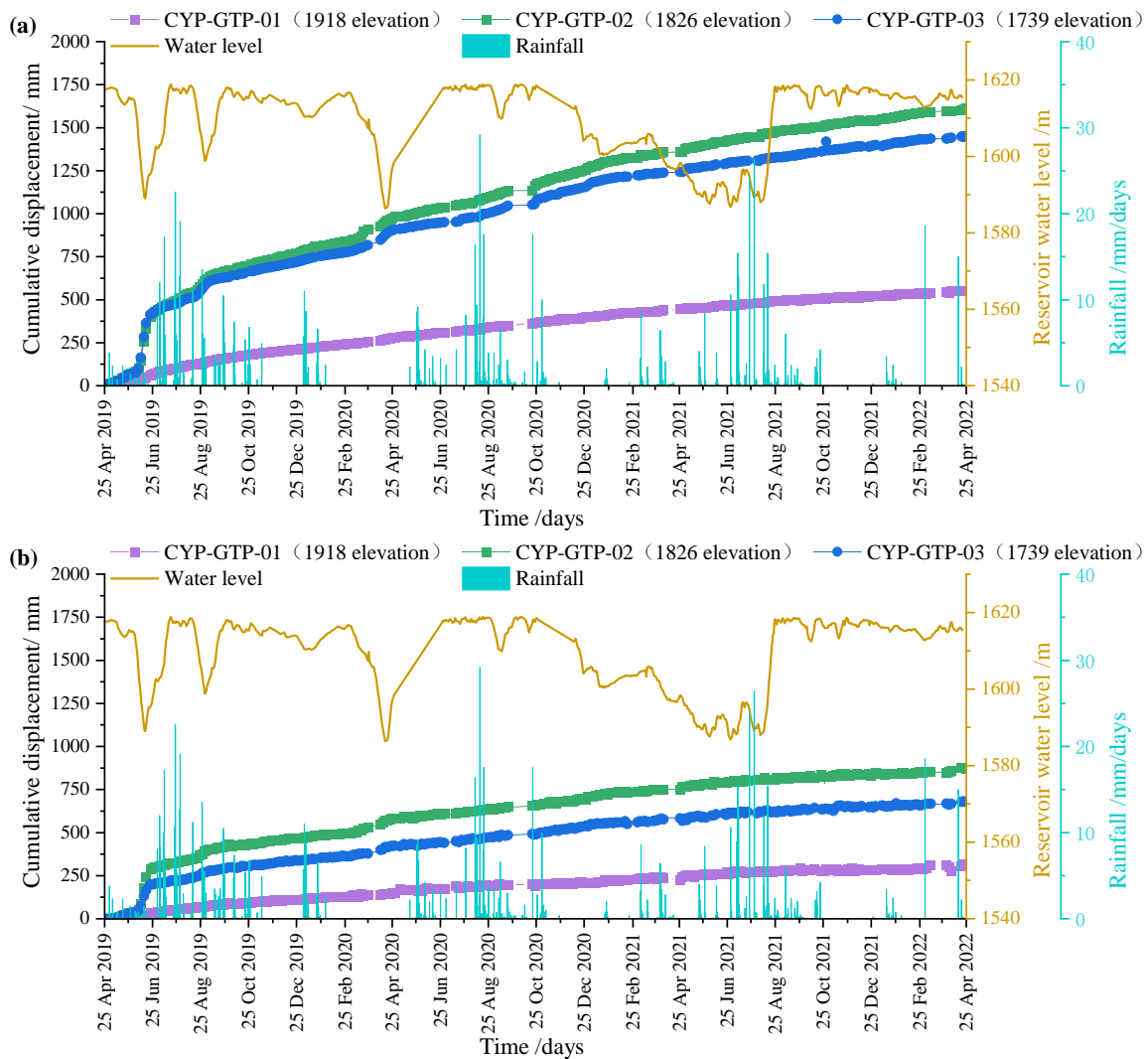


Figure 13. Surface displacement monitoring map: (a) horizontal displacement and (b) vertical displacement.

4.2. Results of Underground Deformation Characterization

Selected monitoring results are illustrated in Figure 14. Incliner boreholes ZK3-5, ZK3-7, and ZK3-9 experienced shear failure at depths of 27 m, 22 m, and 53 m, respectively, on 20 November 2019, 27 December 2019, and 6 March 2020. During the supplementary investigation phase, inclinometer boreholes BZK1-1, BZK1-5, and BZK1-6 completed a total of 21 monitoring cycles. Among these, shear failure occurred at depths of 53.50 m and 26.5 m in BZK1-1 and BZK1-6, respectively, on 9 July 2020, and 19 July 2020.

The five inclinometer boreholes installed in the third phase (CYP-ZK01~CYP-ZK05) completed a total of 8 monitoring cycles. Currently, these inclinometer boreholes are in good operating condition, with no shear failure observed.

Upon a comprehensive analysis of the deformation data from various deep inclinometer boreholes, the deformation characteristics of the landslide are primarily manifested as follows:

(1) Between the elevations of 1805 m and 1619 m along the lower section of the riverside road, monitoring holes show deformation in both shallow and deep parts. Shallow surface deformation is primarily observed between 20 m and 25 m, while deep deformation occurs between 45 m and 50 m. An analysis reveals that the shallow surface deformation is significantly influenced by changes in the reservoir water level, manifesting as arcuate

traction-type deformation. This deformation, characterized by a considerable magnitude, reflects the internal stress adjustment within the landslide to gradually adapt to the changes in the reservoir water level. In contrast, deep deformation represents the landslide’s intrinsic deep-seated creep deformation, with a smaller magnitude.

(2) Data from inclinometer boreholes above 1805 m along the riverside road indicate that the deformation of this section of the landslide mainly concentrates in the depth range of 50 m to 60 m. The analysis suggests that the outer landslide of the riverside road is significantly affected by reservoir storage and water level fluctuations, leading to noticeable displacement. The rear landslide has a high self-weight stress, and the forward deformation of the front landslide causes deformation and failure in the rear landslide, manifesting as intermittent creep deformation of the landslide under specific conditions or triggers.

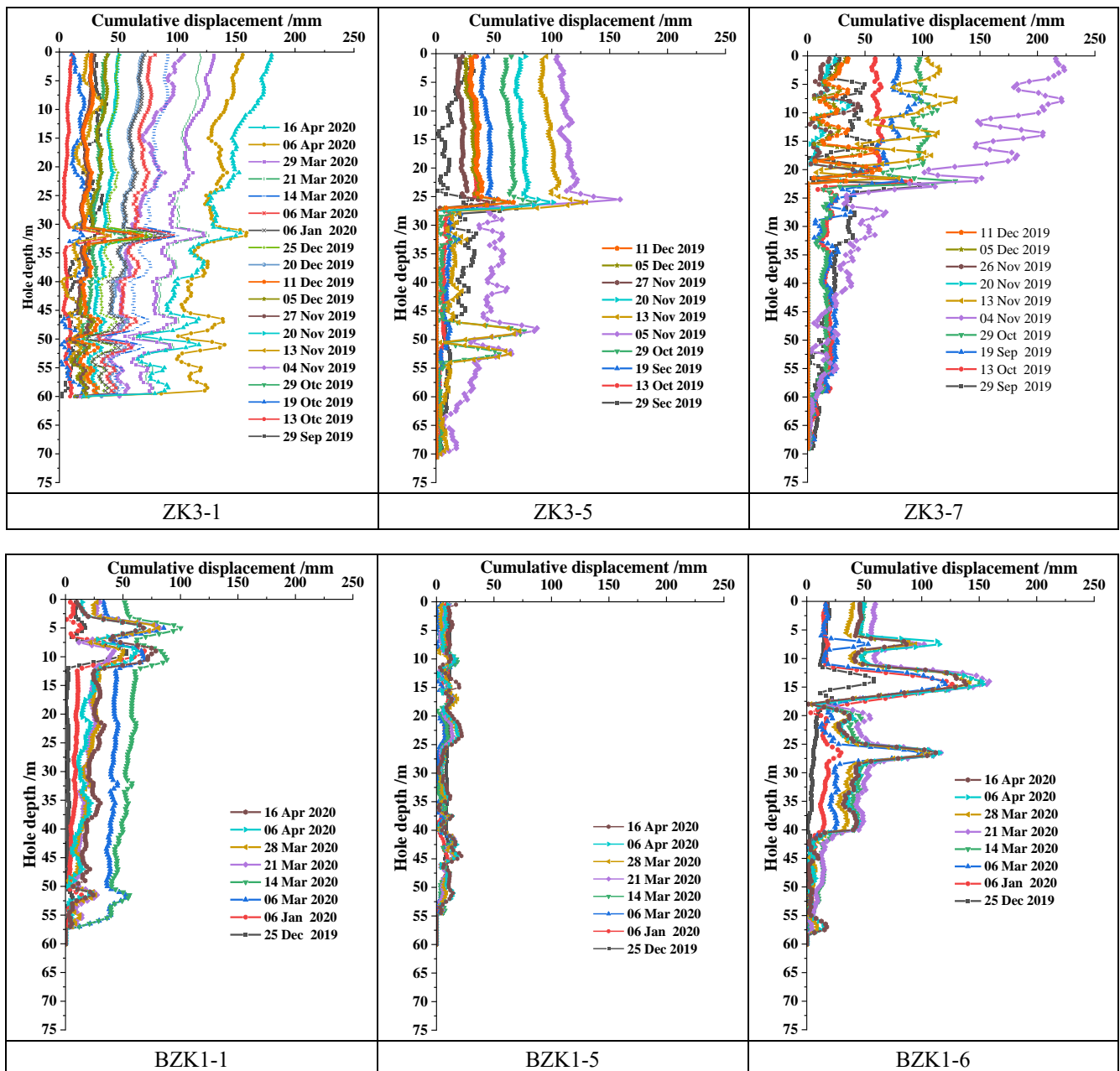


Figure 14. Deep underground displacement monitoring results.

4.3. Correlation between Water-Level Fluctuations and the Reactivation

Due to the varying rates of water level, the displacement of landslides varies accordingly. Therefore, the analysis of the correlation between reservoir water level fluctuations and cumulative displacement is divided into three stages based on the trend of reservoir water level changes: descending, fluctuating, and ascending, as shown in Table 4.

Table 4. Reservoir water level change stages.

Stages (Reservoir Water Level)	Time	Change in Reservoir Water Level (m)
Fluctuating	25 April 2019–30 May 2019	1617–1615
Descending	2 June 2019–19 June 2019	1614–1589
Ascending	19 June 2019–18 July 2019	1589–1618
Fluctuating	19 July 2019–13 August 2019	1618
Descending	14 August 2019–30 August 2019	1617–1598
Ascending	31 August 2019–28 September 2019	1598–1618
Fluctuating	29 September 2019–16 January 2020	1618–1610
Ascending	17 January 2020–29 February 2020	1610–1616
Descending	1 March 2020–15 April 2020	1616–1586
Ascending	17 April 2020–29 June 2020	1586–1617
Fluctuating	30 June 2020–28 August 2020	1617–1618

A quantitative analysis of the correlation between landslide displacement and reservoir water level was conducted using data from 2019 to 2020, resulting in Table 5.

Table 5. Summary of Pearson correlation coefficients between cumulative landslide displacements and water levels.

Scheme	Time	Pearson Correlation Coefficients between Landslide Cumulative Displacement and Reservoir Water Level r		
		CYP-GTP-01	CYP-GTP-02	CYP-GTP-03
Fluctuating	25 April 2019–30 May 2019	0.0289	−0.02736	−0.0480
Descending	2 June 2019–19 June 2019	−0.7185	−0.5056	0.0574
Ascending	19 June 2019–18 July 2019	−0.0614	−0.2178	−0.3409
Fluctuating	19 July 2019–13 August 2019	0.0320	0.0616	0.2167
Descending	14 August 2019–30 August 2019	−0.1932	−0.7105	−0.6748
Ascending	31 August 2019–28 September 2019	0.2430	−0.0899	0.0433
Fluctuating	29 September 2019–16 January 2020	0.03529	−0.06132	0.0386
Ascending	17 January 2020–29 February 2020	0.1039	−0.1146	0.0318
Descending	1 March 2020–15 April 2020	−0.7891	0.2331	−0.8977
Ascending	17 April 2020–29 June 2020	0.0567	0.1740	0.2039
Fluctuating	30 June 2020–28 August 2020	0.1524	0.1410	−0.2441

The correlation coefficients r of deformation monitoring points CYP-GTP-01, CYP-GTP-02, and CYP-GTP-03 on the landslide exhibit a certain level of consistency for the same months. During periods of fluctuating water levels, the deformation of the landslide progresses slowly. However, during decreasing reservoir water levels, as the correlation coefficient $|r|$ increases, the extent of the landslide's deformation in response to changes in the reservoir water level also increases.

However, during each period of decreasing reservoir water levels, there is a discrepancy between one monitoring point and the other two. Analysis suggests that this discrepancy is due to a certain degree of missing data in the monitoring points and reservoir water level data, leading to some calculation errors. During the descending stage, except for individual points, the correlation coefficients between the deformation of various points on the landslide and the reservoir water level can range from -0.8977 to -0.5056 , generally around -0.75 . This indicates a positive correlation and moderate correlation between

the deformation of the landslide and the rapid decrease in reservoir water level. In other words, the faster the reservoir water level decreases, the greater the deformation of the landslide. In other stages, the correlation coefficients between the cumulative displacement of the landslide and the reservoir water level are relatively small, indicating a low degree of correlation, and the deformation of the landslide tends to be smooth, with a low level of response to the reservoir water level.

In this study, we focus on analyzing the correlation between landslide deformation and reservoir water level. However, since rainfall during the period also affects landslide deformation, analyzing only the influence of reservoir water level on landslide deformation may not accurately reflect their complex relationship. To mitigate the influence of rainfall on the relationship between water level and deformation, we control for the rainfall variable.

When computing the correlation between landslide cumulative displacement and reservoir water level fluctuations, rainfall is treated as a control variable. The Pearson correlation coefficients between each factor are computed separately. These coefficients are then used in Equation (2), and the detailed results are presented in Table 6.

Table 6. Summary of net correlation coefficients between cumulative landslide displacements and water levels.

Stages (Reservoir Water Level)	Time	Net Correlation Coefficients between Landslide Cumulative Displacement and Reservoir Water Level r_{12-3}		
		GTP-01	GTP-02	GTP-03
Fluctuating	25 April 2019–30 May 2019	0.0386	−0.0279	−0.0513
Descending	2 June 2019–19 June 2019	−0.7085	−0.5015	0.0578
Ascending	19 June 2019–18 July 2019	−0.0900	−0.1983	−0.3195
Fluctuating	19 July 2019–13 August 2019	−0.0140	0.0926	0.2071
Descending	14 August 2019–30 August 2019	−0.1918	−0.7201	−0.6813
Ascending	31 August 2019–28 September 2019	0.2411	−0.0907	0.0370
Fluctuating	29 September 2019–16 January 2020	0.0303	−0.0667	0.0319
Ascending	17 January 2020–29 February 2020	0.0652	−0.0803	−0.0222
Descending	1 March 2020–15 April 2020	−0.9656	−0.8039	−0.8593
Ascending	17 April 2020–29 June 2020	0.0194	0.1793	0.2114
Fluctuating	30 June 2020–28 August 2020	0.1159	0.1217	−0.2484

When considering rainfall as a control variable in calculating the net correlation between landslides and reservoir water levels, it was observed that during periods of rapid reservoir water level decline, the net correlation coefficient between landslide deformation and reservoir water level is highest, reaching above -0.9 , indicating a high degree of correlation. This suggests that the faster the reservoir water level decreases, the greater the landslide deformation. The period from 1 March 2020, to 15 April 2020, with reservoir water levels between 1616 m and 1586 m, exhibited the highest responsiveness of landslide deformation to reservoir water level changes.

4.4. Stability of the Landslide

The computed results for landslide safety factors under varying water levels are summarized in Table 7. At the normal water level, the stability is relatively high, with a safety factor of 1.062. However, when the water level drops to the dead water level, the safety factor decreases to 1.048. This suggests that a decrease in water level from the normal level to the dead level may trigger landslide instability and failure. This observation aligns with the recent sliding failure characteristics observed at the front edge of the Cheyiping ancient landslide deposit (H_1) in June 2019, which were induced by a sudden drop in reservoir water level to a low level.

Table 7. Landslide safety coefficients at different reservoir levels.

Water Level Status	Groundwater + Reservoir Level	Groundwater + Reservoir Level + Rainfall
Normal water level	1.062	1.062
Dead water level	1.048	1.048

The safety factors under the influence of solely reservoir water level fluctuations and under the combined effects of reservoir water level fluctuations and 30 mm/d rainfall show negligible variation. This indicates that, in this scenario, the fluctuation of the reservoir water level predominantly influences the landslide stability, while the impact of rainfall on the stability of this reservoir bank landslide is minimal.

Figure 15 illustrates saturation maps at varying water levels. It is evident that with the decrease in reservoir water level, there is an overall reduction in the saturation of the soil above the groundwater level. The areas experiencing significant changes are predominantly located near the base of the landslide. Following the decrease in reservoir water level, the zero hydraulic headline exhibits a concave shape, leading to larger unsaturated zones near the base of the landslide.

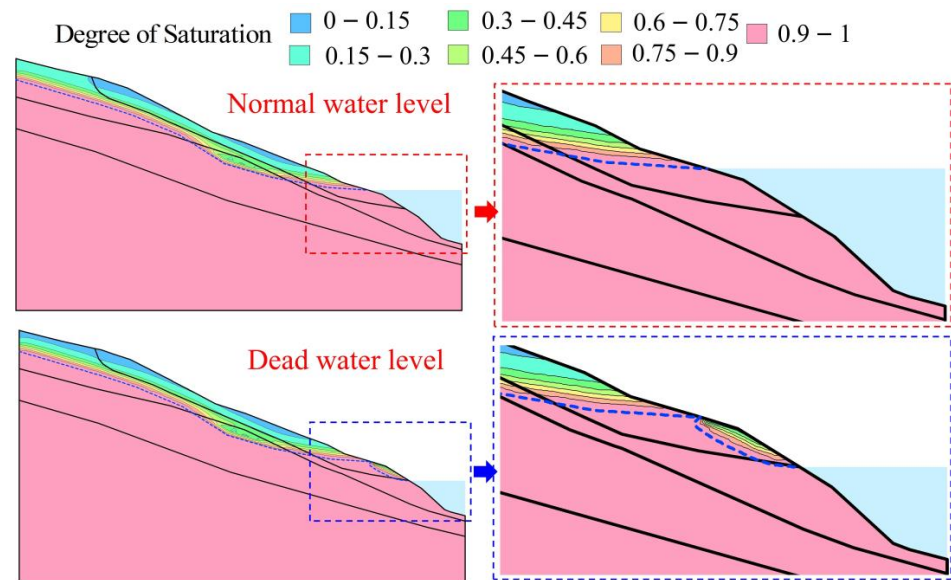


Figure 15. Saturation maps at varying water levels.

Figure 16 illustrates the distribution patterns of pore water pressure and total pressure on the sliding surface (horizontal distribution range approximately 122 m to 608 m) at different reservoir water levels. The figure indicates that reservoir water level fluctuations have a significant impact on the forefront of the landslide (516 m to 608 m). When the reservoir water level decreases from its normal level to its minimum level, both the pore water pressure and total pressure at the forefront of the landslide decrease. However, the influence range of the total pressure is slightly smaller than that of the pore water pressure.

The decline in reservoir water levels has led to a significant reduction in pore water pressure within a 92 m range (516 m to 608 m) and total pressure within a 50 m range (558 m to 608 m). This decrease in pore water pressure results in an increase in the effective stress of the soil mass, consequently enhancing its effective shear strength. However, the declining water level has also caused a reduction in the pressure acting on the landslide surface and directed towards the interior of the landslide, as well as a decrease in the normal stress acting at the base of the sliding mass. These reductions have contributed to an increase in the instability factors of the landslide, leading to a substantial decrease in landslide stability as the reservoir water level decreases.

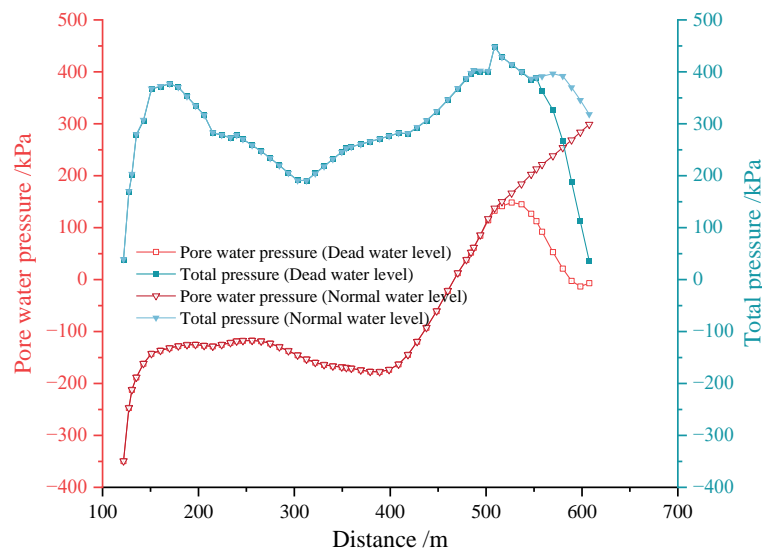


Figure 16. The distribution of pore water pressure and total pressure on the sliding surface at different reservoir water levels.

During April 2019 and April 2022, the of the Huangdeng Reservoir experienced frequent water-level fluctuations. To further explore the temporal evolution of the stability of the reservoir bank landslide, the water level and rainfall intensity data measured during this period were input into a numerical model in Geostudio for computational analysis.

Figure 17 illustrates the temporal variation of the landslide factor of safety. It is evident that there is a strong correlation between the stability of the reservoir bank landslide and the reservoir water level. As the reservoir water level rises and falls, the landslide safety coefficient also increases and decreases accordingly. The greater the fluctuation in reservoir water level, the larger the range of change in the safety coefficient. Under the coupling effect of actual reservoir water level changes and rainfall, the safety coefficient of the reservoir bank landslide is almost identical to that under the condition considering only the effect of reservoir water level changes. This further indicates that the impact of rainfall on the stability of the reservoir bank landslide is minimal, consistent with previous computational results.

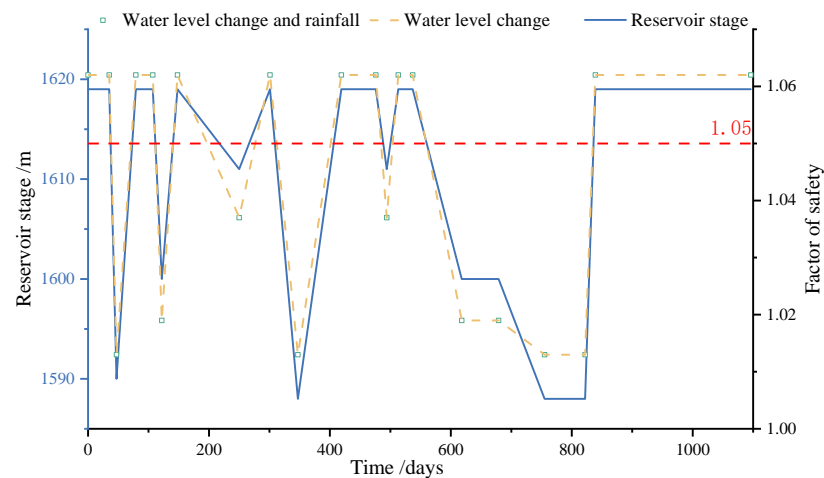


Figure 17. The temporal variation of the landslide factor of safety.

To further investigate the influence of reservoir water level change rates on landslide stability, we conducted an analysis of the stability of reservoir bank landslides under varying rates of reservoir water level rise and fall. In actual conditions, the maximum rate

of reservoir water level decline is approximately 2 m/day. We considered four different scenarios of reservoir water level change: 0.5 m/day, 1 m/day, 1.5 m/day, and 2 m/day. Initially, the reservoir water level was maintained at the normal level for 0–35 days, after which it was lowered to the dead water level at different rates. This level was maintained for a period until the pore water pressure stabilized (147 days), after which the reservoir water level was raised back to the normal level at the same rate as the reservoir water level had dropped.

Figure 18 depicts the variations in landslide safety factors under different rates of reservoir water level change. It reveals a nearly one-to-one correspondence between the landslide safety factor of this project and the elevation of the reservoir water level. The safety factor changes synchronously with the reservoir water level changes, without exhibiting any lag in response to the water level variations. The rate of safety factor change is not uniform, with the fastest changes occurring at the beginning of the reservoir water level decline and at the end of the reservoir water level rise.

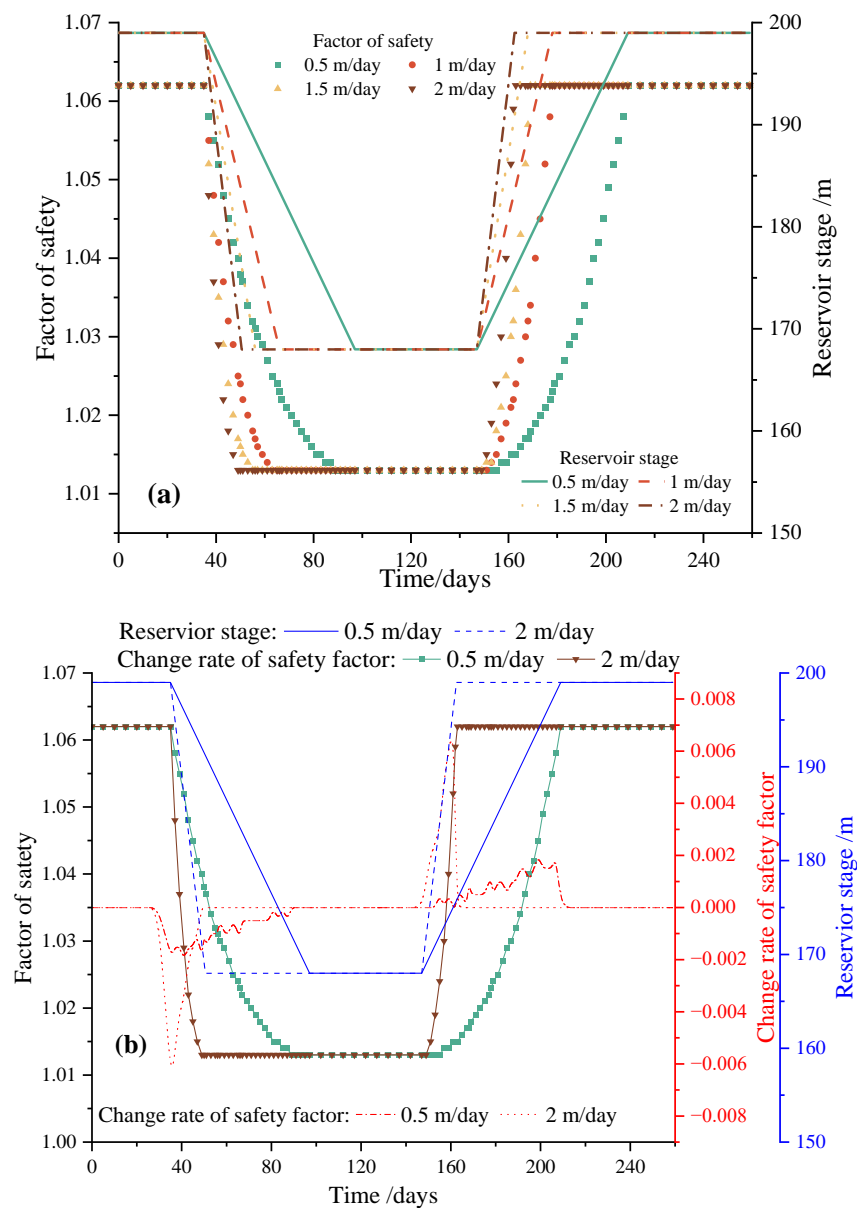


Figure 18. Evolution of landslide stability under different rates of reservoir level change: (a) the evolution of safety factor over time; (b) change rate of safety factor over time.

The aforementioned research indicates that in colluvial deposit landslides containing ancient landslide surfaces with moderate permeability, stability is notably sensitive to reservoir water level fluctuations, while minor rainfall intensities (below 30 mm/d) have virtually no adverse effects. Moreover, in similar practical engineering contexts, particular attention should be given to changes in reservoir water level elevations. Efforts should be made to maintain the water level at a high position to mitigate the potential for landslide instability. Additionally, in cases where reservoir water level adjustments are necessary, it is advisable to implement gradual changes in water level, particularly during initial descent and final ascent, to prevent excessive fluctuations in the landslide safety factor.

5. Revival Mechanism

5.1. Causes of Ancient Landslide Revival

The influence of water on the stability of landslides is notably significant [24,25]. This influence primarily manifests in two aspects. Firstly, water has a softening and liquefying effect on soft rocks, extremely soft rocks, weak interlayers, and fine-grained materials (particularly clay and silt particles), leading to a significant reduction in the strength of rock and soil masses as well as structural surfaces [26]. Secondly, water creates dynamic and static pressures. Infiltration of rainwater and reservoir impoundment elevate the groundwater table, increasing pore water pressure and reducing the landslide's resistance to sliding, thereby causing landslide deformation and failure. Additionally, the discharge of groundwater from the landslide generates dynamic water pressure, intensifying the sliding force along the direction of groundwater flow, which is detrimental to landslide stability [14].

(1) The Influence of Reservoir Water Level Fluctuations

According to our investigation, the primary cause of ancient landslide reactivation in this project is the frequent fluctuation of water levels during reservoir operation. A substantial increase in reservoir water level results in significant water infiltration into the landslide surface, altering its moisture content and simultaneously raising the groundwater level within the landslide. In permeable soil layers, the rate of groundwater level rise often fails to match that of the reservoir, leading to unstable transient seepage within the landslide [27]. The combined effects of transient seepage and water softening result in a significant reduction in the mechanical properties of the rock and soil mass within the landslide. Moreover, the rise in reservoir water level significantly increases water pressure acting on the landslide's outer surface. Determining the dominant factor between these two competing influences requires computational analysis [28].

The surface soil layer on the landslide of this project exhibits a moderate permeability. The rate of groundwater level rise within the slopes is capable of adapting well to the rate of reservoir water level rise. Consequently, the rapid rise of the reservoir water level results in minimal transient seepage effects within the slopes, as the dominant influence is the water head pressure acting on the outside of the slopes. As a result, the slopes ultimately stabilize. Numerical computation results also indicate a significant increase in the slope stability coefficient with the rise of the reservoir water level. Despite the rainy season coinciding with the reservoir impoundment period, a substantial amount of rainfall did not induce slope instability, indicating the limited influence of rainfall in this case. It is noteworthy that the rise in reservoir water levels does not always have a positive effect, as cases of slope instability caused by reservoir impoundment, such as those at the Three Gorges Dam and the Jinping I Hydropower Station, are also common [29,30].

The sudden reduction in reservoir water levels can significantly jeopardize landslide stability. In June 2019, when the reservoir water level began to drop sharply, the ancient landslide at Cheyiping was reactivated. During such events, the inability of the landslide's internal pore water pressure to dissipate promptly leads to the generation of seepage pressure along the direction of sliding. This heightened pressure increases the traction force along the sliding surface, inducing instability and landslide failure. This study also reveals a direct relationship between the safety factor of the landslide and the fluctuations

in reservoir water levels, with a notable decrease in the safety factor as the reservoir water level decreases. This observation suggests that the project falls under the classification of seepage-induced landslides [31]. Throughout the fluctuation of reservoir water levels, the dominant role of seepage force ultimately culminates in landslide failure during the lowering of the reservoir water levels [26].

(2) The Impact of Rainfall

This study also includes an analysis of the impact of rainfall on reservoir bank slopes. It is widely recognized that heavy rainfall has a significant influence on the sliding deformation and damage of reservoir areas. On one hand, heavy rainfall leads to a substantial infiltration of rainwater into the slope, increasing the saturation of the soil within the slope and thereby enhancing the delayed water pressure response effect. On the other hand, as the water level decreases, the negative pore water pressure at the front edge of the slope increases, intensifying the infiltration of rainwater. This, in turn, leads to an increased likelihood of oversaturation in the shallow layers of the slope, thereby increasing the factors contributing to slope instability [32]. However, relative to the influence of water level fluctuations, rainfall's effect in this project is minimal. This is attributed to the moderate permeability of the project area's landslide surface and the relatively low actual intensity of rainfall, which further mitigates rainfall's adverse effects on the landslide.

Zhang [33] conducted an in-depth analysis of the impact of rainfall on the reactivation of accumulated landslide bodies using centrifuge model tests and numerical simulation methods. The study revealed that the permeability of ancient landslide bodies is generally weak, making it challenging for conventional rainfall to infiltrate deep into the body and trigger large-scale reactivation. The research also indicates that rainfall is not a direct factor in inducing the reactivation of ancient landslides. In this case, the rapid decrease in reservoir water level was the direct trigger for the reactivation of the ancient landslide. Following the rise in reservoir water level, the submerged front edge of the slope underwent prolonged soaking, leading to a reduction in its shear strength. The subsequent rapid decrease in reservoir water level induced pore pressure within the slope along the direction of sliding. Given that the slope surface mainly consists of sand and silt, its ability to support the slope was limited, ultimately resulting in sliding failure at the front edge of the slope.

Consequently, the actual impact of rainfall on landslide stability in this project can be largely disregarded, with the deformation and failure of the landslide primarily attributed to declining water levels.

5.2. Characteristics of Ancient Landslide Reactivation and Destruction

In this project, similar to many landslide engineering endeavors within reservoir areas, landslides (H_{1-3}) occurred in proximity to zones characterized by frequent water level fluctuations [10,34]. Notably, despite the presence of weakened surfaces from ancient landslides, the landslides did not reactivate along these existing surfaces under the influence of reservoir water levels. Instead, new arc-shaped slip surfaces formed at the leading edge of the landslide, resulting in localized collapse and damage. Subsequent sliding deformation extended further rearward, inducing the development of multiple tension cracks along the landslide's trailing edge. This observation suggests that the impact of reservoir water level changes on the landslide is limited, insufficient to directly trigger extensive landslide reactivation along the original slip surfaces. Nevertheless, the fluctuations in reservoir water levels remain consequential, as they can readily provoke sliding at the forefront of reservoir bank landslides, indirectly precipitating traction-type landslides on the landslide. Should the ancient landslide's sliding surface exhibit low strength, a traction-type slide along the ancient sliding surface becomes highly probable, culminating in the reactivation of the ancient landslide. Numerous studies have indicated that rainfall can quickly infiltrate the sliding zone through tension cracks at the rear of the slope. This infiltration reduces the shear strength of the sliding zone, thereby increasing the likelihood of traction-induced sliding failure [35–37].

6. Conclusions

The Cheyiping landslide project experienced a significant deformation in June 2019, resulting in extensive ground cracking along the reservoir bank, as well as cracking and subsidence of houses and foundations in nearby villages and partial collapse of the riverside road. Through long-term monitoring, field investigations, and theoretical analysis, the study focused on its distribution characteristics, damage features, and the mechanism of ancient landslide reactivation, yielding the following main conclusions:

(1) Monitoring data from the landslide surface indicates that the rate of deformation during reservoir water level decrease is significantly greater than during water level rise, suggesting a notable impact of water level decrease on the landslide surface. Internal monitoring data reveals pronounced deformations in both shallow and deep layers at the landslide's front, exhibiting a "circular-arc" sliding pattern. In contrast, sliding deformations at the rear of the landslide primarily occur in the shallow layers, displaying a "tilt" sliding pattern. This suggests that, in this project, the landslide experiences local instability at the front, weakening the support to the rear and leading to traction-type sliding deformation and collapse toward the reservoir bank.

(2) The correlation analysis of the reservoir water level indicates a strong relationship between the decrease in water level and the cumulative deformation of the landslide. The faster the decrease in reservoir water level, the greater the cumulative deformation of the landslide. In contrast, the correlation between the increase in reservoir water level and the cumulative deformation of the landslide is weaker.

(3) Numerical simulations reveal that the stability coefficient of the landslide rises with increasing reservoir water levels and falls as they decrease. The primary factor influencing landslide stability is the reservoir water level, while the impact of rainfall on landslide stability is negligible. The rate of change in the landslide's stability coefficient is most pronounced during the initial stages of reservoir water level decline and the final stages of water level rise. Fluctuations in reservoir water levels can induce slope instability, warranting long-term monitoring and inspection of slope deformation. It is advisable that during reservoir management, water levels be lowered gradually, while closely monitoring slope deformation during these periods. If necessary, reinforcement should be applied to the slope's forefront to directly support its rear. Additionally, any cracks on the slope should be promptly filled or fitted with waterproofing membranes and drainage channels to prevent rainwater from infiltrating the sliding zone, despite rainfall not being the direct trigger for the reactivation of ancient landslides in this case.

In summary, the stability of reservoir bank landslides is closely intertwined with reservoir water levels. The decrease in water levels poses the greatest risk factor for inducing traction-type sliding failures in the ancient Cheyiping landslide, while the influence of rainfall is relatively minor in this project.

Author Contributions: L.D.: Writing—original draft. C.J.: Visualization, Investigation. L.C.: Formal analysis. Q.Z.: Visualization, Investigation. W.C.: Formal analysis. All authors have read and agreed to the published version of the manuscript.

Funding: This work presented in this paper was financially supported by the National Natural Science Foundation of China (Grant No. 52378421).

Institutional Review Board Statement: Not applicable.

Informed Consent Statement: Not applicable.

Data Availability Statement: All data, models, and code that support the findings of this study are available from the corresponding author upon reasonable request.

Conflicts of Interest: Author Wei Chen was employed by the PowerChina Kunming Engineering Corporation Limited. The remaining authors declare that the research was conducted in the absence of any commercial or financial relationships that could be construed as a potential conflict of interest.

References

1. GB T 32864–2016; Code for Geological Investigation of Landslide Prevention. China Standardization Press: Beijing, China, 2016.
2. Nilsen, T.H.; Turner, B.L. *Influence of Rainfall and Ancient Landslide Deposits on Recent Landslides (1950–71) in Urban Areas of Contra Costa County, California*; U.S. Government Printing Office: Sacramento, CA, USA, 1975.
3. Di Maio, C.; Vassallo, R.; Vallario, M.; Pascale, S.; Sdao, F. Structure and kinematics of a landslide in a complex clayey formation of the Italian Southern Apennines. *Eng. Geol.* **2010**, *116*, 311–322. [[CrossRef](#)]
4. Dykes, A.P.; Bromhead, E.N. The Vaiont landslide: Re-assessment of the evidence leads to rejection of the consensus. *Landslides* **2018**, *15*, 1815–1832. [[CrossRef](#)]
5. Polemio, M.; Sdao, F. The role of rainfall in the landslide hazard: The case of the Avigliano urban area (Southern Apennines, Italy). *Eng. Geol.* **1999**, *53*, 297–309. [[CrossRef](#)]
6. Voight, B.; Faust, C. Frictional heat and strength loss in some rapid landslides: Error correction and affirmation of mechanism for the Vaiont landslide. *Geotechnique* **1992**, *42*, 641–643. [[CrossRef](#)]
7. Superchi, L.; Floris, M.; Ghirotti, M.; Genevois, R.; Jaboyedoff, M.; Stead, D. Implementation of a geodatabase of published and unpublished data on the catastrophic Vaiont landslide. *Nat. Hazards Earth Syst. Sci.* **2010**, *10*, 865–873. [[CrossRef](#)]
8. Del Ventisette, C.; Gigli, G.; Bonini, M.; Corti, G.; Montanari, D.; Santoro, S.; Sani, F.; Fanti, R.; Casagli, N. Insights from analogue modelling into the deformation mechanism of the Vaiont landslide. *Geomorphology* **2015**, *228*, 52–59. [[CrossRef](#)]
9. Zhu, D. Revival Mechanism and Deformation Prediction of Typical Accumulative Landslide in the Three Gorges Reservoir. Master's Thesis, China University of Geoscience, Wuhan, China, 2010.
10. Tang, H.; Wasowski, J.; Juang, C.H. Geohazards in the three Gorges Reservoir Area, China—Lessons learned from decades of research. *Eng. Geol.* **2019**, *261*, 105267. [[CrossRef](#)]
11. Yin, Y.-p.; Huang, B.; Chen, X.; Liu, G.; Wang, S. Numerical analysis on wave generated by the Qianjiangping landslide in Three Gorges Reservoir, China. *Landslides* **2015**, *12*, 355–364. [[CrossRef](#)]
12. Wang, J.; Wang, S.; Su, A.; Xiang, W.; Xiong, C.; Blum, P. Simulating landslide-induced tsunamis in the Yangtze River at the Three Gorges in China. *Acta Geotech.* **2021**, *16*, 2487–2503. [[CrossRef](#)]
13. Dong, Y.; Liao, Z.; Wang, J.; Liu, Q.; Cui, L. Potential failure patterns of a large landslide complex in the Three Gorges Reservoir area. *Bull. Eng. Geol. Environ.* **2023**, *82*, 41. [[CrossRef](#)]
14. Jia, C.; Chen, F.; Zhang, Q.; GU, J.; Hu, J.; Chen, H.; Cheng, W. Centrifuge modeling and numerical analysis of reservoir bank landslides triggered by a fast two-step drop in water level. *Bull. Eng. Geol. Environ.* **2023**, *82*, 465. [[CrossRef](#)]
15. Rana, N.M.; Ghahramani, N.; Evans, S.G.; Small, A.; Skermer, N.; McDougall, S.; Take, W.A. Global magnitude–frequency statistics of the failures and impacts of large water-retention dams and mine tailings impoundments. *Earth-Sci. Rev.* **2022**, *232*, 104144. [[CrossRef](#)]
16. Wang, L.; Zhang, Z.; Huang, B.; Hu, M.; Zhang, C. Triggering mechanism and possible evolution process of the ancient Qingshi landslide in the Three Gorges Reservoir. *Geomat. Nat. Hazards Risk* **2021**, *12*, 3160–3174. [[CrossRef](#)]
17. Huang, B.; Yin, Y.; Tan, J. Risk assessment for landslide-induced impulse waves in the Three Gorges Reservoir, China. *Landslides* **2019**, *16*, 585–596. [[CrossRef](#)]
18. GB 50287–2016; Code for Hydropower Engineering Geological Investigation. China Standardization Press: Beijing, China, 2016.
19. Rahadian, H.; Bandong, S.; Widyotriatmo, A.; Joeliyanto, E. Image encoding selection based on Pearson correlation coefficient for time series anomaly detection. *Alex. Eng. J.* **2023**, *82*, 304–322. [[CrossRef](#)]
20. Gao, H.X.; Yin, K.L. Discuss on the correlations between landslides and rainfall and threshold for landslide early-warning and prediction. *Rock Soil Mech.* **2007**, *28*, 1055–1060.
21. Van Aert, R.C.; Goos, C. A critical reflection on computing the sampling variance of the partial correlation coefficient. *Res. Synth. Methods* **2023**, *14*, 520–525. [[CrossRef](#)]
22. Shang, M.; Liao, F.; Ma, R.; Liu, Y. Quantitative correlation analysis on deformation of Baijiabao landslide between rainfall and reservoir water level. *J. Eng. Geol.* **2021**, *29*, 9.
23. Fredlund, D.G.; Xing, A.; Fredlund, M.; Barbour, S. The relationship of the unsaturated soil shear strength to the soil-water characteristic curve. *Can. Geotech. J.* **1996**, *33*, 440–448. [[CrossRef](#)]
24. Chen, M.L.; Lv, P.F.; Zhang, S.L.; Chen, X.Z.; Zhou, J.W. Time evolution and spatial accumulation of progressive failure for Xinhua slope in the Dagangshan reservoir, Southwest China. *Landslides* **2018**, *15*, 565–580. [[CrossRef](#)]
25. Zhou, J.-w.; Lu, P.-y.; Yang, Y.-c. Reservoir landslides and its hazard effects for the hydropower station: A case study. In *Advancing Culture of Living with Landslides: Volume 2 Advances in Landslide Science*; Springer: Berlin/Heidelberg, Germany, 2017; pp. 699–706.
26. Jiang, J.-w.; Xiang, W.; Rohn, J.; Zeng, W.; Schleier, M. Research on water–rock (soil) interaction by dynamic tracing method for Huangtupo landslide, Three Gorges Reservoir, PR China. *Environ. Earth Sci.* **2015**, *74*, 557–571. [[CrossRef](#)]
27. Belew, A.Z.; Tenagashaw, D.Y.; Ayele, W.T.; Andualem, T.G. Coupled analysis of seepage and slope stability: A case study of ribb embankment dam, Ethiopia. *Water Conserv. Sci. Eng.* **2022**, *7*, 293–314. [[CrossRef](#)]
28. Zhou, J.; Chen, M.; Li, H.; Xu, N.; Xiao, M.; Yang, X.; Sun, H.; QI, S. Formation and Movement Mechanisms of Water-Induced Landslides and Hazard Prevention And Mitigation Technologies. *J. Eng. Geol.* **2019**, *27*, 1131–1145.
29. Xiang, J.; Tang, H. Failure Mechanism Study for Fairy-River Shore Slope in the Three Gorges Reservoir Caused by Water-Impoundment. *J. Chongqing Jiaotong Univ. (Nat. Sci.)* **2011**, *30* (Suppl. S1), 700–704.

30. Chen, C.; Yang, J.; Liu, Z. Mechanism of Reservoir Bank Deformation and Failure in Jinping I Hydropower Project after Impoundment. *Chin. J. Undergr. Space Eng.* **2019**, *15*, 622–628.
31. Pajalić, S.; Peranić, J.; Maksimović, S.; Čeh, N.; Jagodnik, V.; Arbanas, Ž. Monitoring and Data Analysis in Small-Scale Landslide Physical Model. *Appl. Sci.* **2021**, *11*, 5040. [[CrossRef](#)]
32. Zhang, Z.; Zeng, R.; Meng, X.; Zhao, S.; Wang, S.; Ma, J.; Wang, H. Effects of changes in soil properties caused by progressive infiltration of rainwater on rainfall-induced landslides. *Catena* **2023**, *233*, 107475. [[CrossRef](#)]
33. Zhang, Y.; Wu, R.; Ren, S. Influence of rainfall preponderance infiltration path on reactivation of ancient landslides. *Chin. J. Rock Mech. Eng.* **2021**, *40*, 777–789.
34. Li, S.; Xu, Q.; Tang, M.; Zhu, D. Study on Spatial Distribution and Key Influencing Factors of Landslides in Three Gorges Reservoir Area. *Earth Sci.* **2020**, *45*, 341–354.
35. Zhang, C.; Yin, Y.; Dai, Z.; Huang, B.; Zhang, Z.; Jiang, X.; Tan, W.; Wang, L. Reactivation mechanism of a large-scale ancient landslide. *Landslides* **2021**, *18*, 397–407. [[CrossRef](#)]
36. Yang, H.; Song, K.; Chen, L.; Qu, L. Hysteresis effect and seasonal step-like creep deformation of the Jiuxianping landslide in the Three Gorges Reservoir region. *Eng. Geol.* **2023**, *317*, 107089. [[CrossRef](#)]
37. Zhang, C.; Yin, Y.; Yan, H.; Li, H.; Dai, Z.; Zhang, N. Reactivation characteristics and hydrological inducing factors of a massive ancient landslide in the three Gorges Reservoir, China. *Eng. Geol.* **2021**, *292*, 106273. [[CrossRef](#)]

Disclaimer/Publisher’s Note: The statements, opinions and data contained in all publications are solely those of the individual author(s) and contributor(s) and not of MDPI and/or the editor(s). MDPI and/or the editor(s) disclaim responsibility for any injury to people or property resulting from any ideas, methods, instructions or products referred to in the content.